
White Rose Research Online

eprints@whiterose.ac.uk
https://eprints.whiterose.ac.uk
Universities of Leeds, Sheffield and York

Deposited via The University of York.

White Rose Research Online URL for this paper:
https://eprints.whiterose.ac.uk/id/eprint/247403/

Version: Published Version

Article:
Lonsdale, C. M., McHardy, J. D., Storm, C. V. et al. (2026) Structure of niobium to 365 GPa using ultrafast x-ray diffraction and shock compression. Physical Review B. 154101. ISSN: 2469-9969

https://doi.org/10.1103/TLXW-BFX4

Reuse
This article is distributed under the terms of the Creative Commons Attribution (CC BY) licence. This licence allows you to distribute, remix, tweak, and build upon the work, even commercially, as long as you credit the authors for the original work. More information and the full terms of the licence here: https://creativecommons.org/licenses/

Takedown
If you consider content in White Rose Research Online to be in breach of UK law, please notify us by emailing eprints@whiterose.ac.uk including the URL of the record and the reason for the withdrawal request.





Structure of niobium to 365 GPa using ultrafast x-ray diffraction and shock compression

C. M. Lonsdale,[1,*] J. D. McHardy,[1] C. V. Storm,[1] M. I. McMahon,[1,†] R. S. McWilliams,[1] N. Jaisle,[1] M. Jones,[1] C. R. Roy,[1] R. F. Smith,[2] A. Descamps,[3] A. Higginbotham,[4] T. M. Hutchinson,[2] S. Pandolfi,[5] A. Sollier,[6,7] A. Amouretti,[8] M. Andrzejewski,[9] K. Appel,[9] T. Aughey,[3] P. Avery,[10] E. Barraud,[6] A. B. Belonoshko,[11,12] E. Brambrink,[9] N. Bruzy,[6,7] K. Buakor,[9] S. D. Di Dio Cafiso,[13] C. Camarda,[9] O. Castelnau,[14] A. Chakraborti,[15] J. Chantel,[15] D. M. Cheshire,[4] G. W. Collins,[16] A. J. Comley,[17] T. E. Cowan,[13] C. Crépisson,[18] Y. Deng,[19] L. Dresselhaus-Marais,[20,21] X. Fang,[19] M. D. Fitzgerald,[18] S. Galitskiy,[22] E. Galtier,[21] H. Ginestet,[15] J. M. Gonzalez,[22] F. Hanby,[22] A. Hari,[20,21] M. Harmand,[23] N. J. Hartley,[21] P. G. Heighway,[18] J-A. Hernandez,[24] H. Höppner,[13] D. Khaghani,[21] J. Kim,[25] T. Kim,[26] Z. Konôpková,[9] D. Kraus,[13,27] A. Krygier,[2] H. J. Lee,[21] S-N. Luo,[19] M. Masruri,[13] E. E. McBride,[3] D. McGonegle,[17] S. Merkel,[15] T. Michelat,[9] E. Mijit,[24] M. Nakatsutsumi,[9] A-M. Norton,[4] I. K. Ocampo,[2] I. I. Oleynik,[22] C. Otzen,[28] N. Ozaki,[8] S. E. Parsons,[20,21] D. J. Peake,[18] A. Pelka,[13] K. A. Pereira,[29] A. Phelipeau,[28,30] C. Prescher,[28] T. R. Preston,[9] N. Pulver,[2] D. Riley,[3] L. Rogal,[31] J-P. Schwinkendorf,[13] G. Shoulga,[13] S. Singh,[2] C. N. Somarathna,[22] T. Stevens,[18] C. Strohm,[30] T-A. Suer,[16] M. X. Tang,[9] A. Tipeev,[22] M. Toncian,[13] T. Toncian,[13] S. J. Tracy,[32] U. Trdan,[33] J. D. Tunacao,[22] J. D. Umpleby-Thorp,[4] C. E. Vennari,[2] L. Wang,[19] J. S. Wark,[18] C. McGuire,[2] G. Morard,[5] and J. H. Eggert[2]

[1]*SUPA, School of Physics and Astronomy, and Centre for Science at Extreme Conditions, The University of Edinburgh, Peter Guthrie Tait Road, Edinburgh EH9 3FD, United Kingdom*

[2]*Lawrence Livermore National Laboratory, Livermore, California 94550, USA*

[3]*School of Mathematics and Physics, Queen's University Belfast, University Road, Belfast BT7 1NN, United Kingdom*

[4]*York Plasma Institute, School of Physics, Engineering and Technology, University of York, York YO10 5DD, United Kingdom*

[5]*Sorbonne Université, Muséum National d'Histoire Naturelle, UMR CNRS 7590, Institut de Minéralogie, de Physique, des Matériaux, et de Cosmochimie, IMPMC, 75005 Paris, France*

[6]*CEA, DAM, DIF 91297 Arpajon Cedex, France*

[7]*Université Paris-Saclay, CEA, LMCE, 91680 Bruyères-le-Châtel, France*

[8]*Graduate School of Engineering, University of Osaka, 2-1 Yamada-oka, Suita, Osaka 565-0871, Japan*

[9]*European XFEL, Holzkoppel 4, 22869 Schenefeld, Germany*

[10]*Kitware, Inc., Clifton Park, New York 12065, USA*

[11]*Frontiers Science Center for Critical Earth Material Cycling, School of Earth Sciences and Engineering, Nanjing University, Nanjing 210023, China*

[12]*Condensed Matter Theory, Department of Physics, AlbaNova University Center, Royal Institute of Technology (KTH), 10691 Stockholm, Sweden*

[13]*Helmholtz-Zentrum Dresden-Rossendorf (HZDR), Bautzner Landstraße 400, 01328 Dresden, Germany*

[14]*CNRS-DSI Meudon, Laboratoire PIMM (UMR 8006), ENSAM/CNAM, 155 Bd de l'hopital, 75013 Paris, France*

[15]*Univ. Lille, CNRS, INRAE, Centrale Lille, UMR 8207-UMET-Unité Matériaux et Transformations, F-59000 Lille, France*

[16]*Laboratory for Laser Energetics (LLE), University of Rochester, 250 East River Road, Rochester, New York 14623-1299, USA*

[17]*AWE, Aldermaston, Reading RG7 4PR, United Kingdom*

[18]*Department of Physics, Clarendon Laboratory, University of Oxford, Parks Road, Oxford OX1 3PU, United Kingdom*

[19]*School of Materials Science and Engineering, Southwest Jiaotong University, No. 111, North 1st Section of Second Ring Road, Jinniu District, Chengdu City, Sichuan Province, People's Republic of China*

[20]*Stanford Department of Materials Science and Engineering, 476 Lomita Mall, Stanford, California 94025, USA*

[21]*SLAC National Accelerator Laboratory, 2575 Sand Hill Road, Menlo Park, California 94025, USA*

[22]*Department of Physics, University of South Florida, Tampa, Florida 33620, USA*

[23]*PIMM, CNRS, Arts et Metiers Institute of Technology, CNAM, Paris, France*

[24]*European Synchrotron Radiation Facility-ESRF, 71, avenue des Martyrs CS 40220, 38043 Grenoble Cedex 9, France*

[25]*Hanyang University, Department of Physics, 17 Haengdang dong, Seongdong gu Seoul, Korea 133-791, South Korea*

[26]*School of Earth and Space Exploration, Arizona State University, Tempe, Arizona 85287, USA*

[27]*Universität Rostock, Institut für Physik, 18051 Rostock, Germany*

[28]*Institut für Geo- und Umweltnaturwissenschaften, Albert-Ludwigs-Universität Freiburg, Hermann-Herder-Straße 5, 79104 Freiburg, Germany*

[*]Contact author: c.m.lonsdale@sms.ed.ac.uk

[†]Contact author: m.i.mcmahon@ed.ac.uk

Published by the American Physical Society under the terms of the Creative Commons Attribution 4.0 International license. Further distribution of this work must maintain attribution to the author(s) and the published article's title, journal citation, and DOI.

[29]*Department of Chemistry, University of Massachusetts Amherst, 690 N Pleasant Street Physical Sciences Building, Rm 173 Amherst, Massachusetts 01003-9303, USA*
[30]*Deutsches Elektronen-Synchrotron DESY, Notkestrasse 85, 22607 Hamburg, Germany*
[31]*Polish Academy of Sciences, Institute of Metallurgy and Materials Science, Reymonta 25, 30-059 Krakow, Poland*
[32]*Carnegie Science, Earth and Planets Laboratory, 5241 Broad Branch Road, NW, Washington, DC 20015, USA*
[33]*Faculty of Mechanical Engineering, University of Ljubljana, Askerceva 6, 1000 Ljubljana, Slovenia*

(Received 30 December 2025; revised 3 July 2026; accepted 14 July 2026; published 1 September 2026)

The phase stability, crystal structure, and melting of Nb have been examined under high pressure shock compression to 365 GPa using ultrafast *in situ* x-ray diffraction measurements on two x-ray free electron laser facilities. On compression, Nb remains stable in the bcc phase up to 220 GPa, with coexistence of bcc-Nb and liquid from 249 to 298 GPa, and complete melting at 301 GPa, with melt identified by diffuse liquid diffraction. Melting initiates at higher pressure than expected based on theoretical predictions, and the data consistently excludes the presence of other suggested phases of Nb at these pressures, including *Pnma* and hcp, thereby resolving the long-standing structural discrepancy. Singh-type strength analysis provides experimental evidence for a change in sign of the elastic anisotropy parameter at 121 GPa, consistent with the previously reported heat-induced hardening to heat-induced softening transition in Nb.

DOI: 10.1103/tlxw-bfx4

I. INTRODUCTION

Niobium (Nb) is a group VB metal situated between zirconium and molybdenum in the periodic table. Because of its high melting point, chemical inertness, and strength properties, Nb is widely used in industrial applications. These applications include high-entropy alloys [1,2], superconducting magnets for fusion research [3], medical imaging [3], and energy storage technologies [4,5]. Nb exhibits unusual elastic behavior, including atypical softening [6], under high pressure [7–9], which has motivated extensive studies at room temperature using both experimental [6,10–15] and computational techniques [9,16–19]. Given niobium's role in high-performance alloys and fusion reactors, surprisingly few studies have explored its behavior under high pressure and temperature [20–23], in contrast to other body centered-cubic (bcc) metals such as V [24–28], Mo [24,29–33], Ta [34–39], and W [24–26,40,41].

Early shock compression work on Nb, by Al'tshuler *et al.* [42], reported a second-order phase transition at ∼94 GPa, as inferred from a change in the gradient of the shock-velocity versus particle-velocity curve (Supplemental Material Sec. A [43]). Further studies failed to reach sufficient pressures to observe this phase transition [25,26,67], while subsequent molecular dynamics simulations along the principal Hugoniot predicted a solid-solid phase transition from bcc to hexagonal close-packed (hcp) at ∼75 GPa [68]. This pressure is consistent with the dramatic stiffening of the C_{44} elastic constant in Nb previously reported by Koči *et al.* [7] at 300 K and has been considered as the driving mechanism for structural changes in V at high pressure [69]. More recently, Errandonea *et al.* [23], using static-compression techniques, combined laser-heating x-ray diffraction (XRD) and computation to investigate the phase stability, including melting, to ∼60 GPa and ∼3300 K on Nb. They reported a solid-solid transition from bcc to an orthorhombic *Pnma* structure some 1000–1500 K prior to melting. Extension of the experimental results to higher pressures using *ab initio* molecular dynamical simulations suggested the transition to the orthorhombic phase would occur at ∼142 GPa along the principal Hugoniot [23]. The existence of intermediate solid phases of Nb and the onset of melting remain unresolved, with conflicting predictions and static results, motivating our ultrafast shock compression measurements.

Significant progress in generating and studying extreme pressure-temperature (*P*-*T*) states through dynamic compression and XRD has been made over the past decade [36,70–75]. In some instances, these methods couple long pulse (∼10 ns), high-energy drive lasers with the extreme brightness of modern x-ray free-electron lasers (XFELs) [76–79]. The new DiPOLE 100-X laser [80,81], at the High Energy Density (HED) instrument of the European x-ray Free Electron Laser (EuXFEL) [82], and the long-pulse laser system at the Matter in Extreme Conditions (MEC) end station of the Linac Coherent Light Source (LCLS) [83], enable ultrafast *in situ* XRD studies along the principal Hugoniot with fine temporal control.

In this paper, we apply these technologies at HED and MEC to shock compress Nb to extreme states and carry out *in situ* crystal structure investigations using XRD with femtosecond time resolution, resolving the structural controversy of Nb along the principal Hugoniot. We present diffraction data for solid-bcc and liquid Nb up to a maximum pressure of 365(32) GPa. The data set comprises twenty two shots from solid Nb, six shots along the melt curve showing coexistence of solid and liquid phases, and two shots from fully molten Nb. We observe clear evidence of the incipient melting of Nb at a pressure of 249(41) GPa, as determined from a reduction in Bragg peak intensities and the appearance of a strong diffuse scattering signal from the liquid phase. Prior to the onset of melting, we find no evidence of the previously reported bcc → hcp or bcc → *Pnma* solid-solid transitions [23,68]. Our results establish the structural response of Nb along the principal Hugoniot, quantify the melt boundary, and reveal a change in sign of the elastic anisotropy parameter, *S*.

II. EXPERIMENTAL METHODS

The experiments were carried out during two campaigns at different XFEL facilities. The first was conducted in

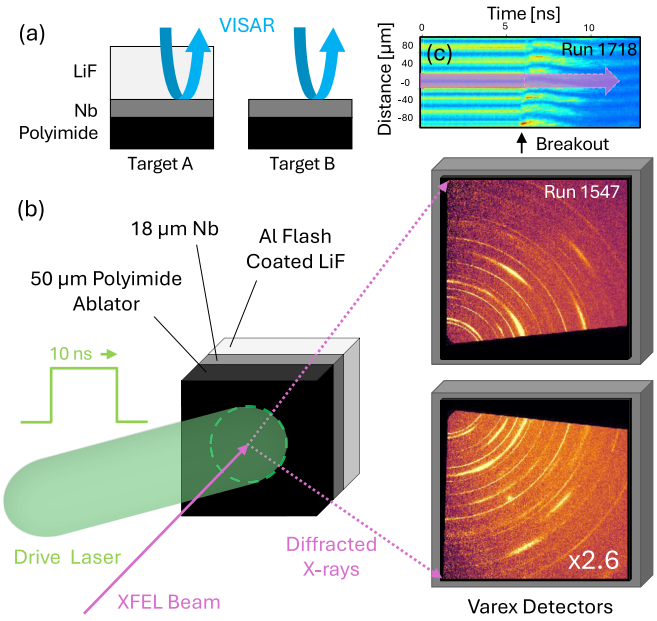


FIG. 1. (a) The two target types shot during this experiment indicated by targets A and B. (b) Schematic of the experimental setup used to collect VISAR and *in situ* XRD data at HED and MEC, not to scale. VISAR measured the particle velocity at the Al-LiF interface of the A-type targets. The two Varex detectors on HED enable approximately half of the Debye-Scherrer XRD pattern to be collected, and an example 2D diffraction image from laser-shocked Nb at 82(26) GPa (Run 1547 HED) is shown with ×2.6 magnification. (c) Representative VISAR image for a type-A target (Run 1718 HED). The pink arrow indicates the width of the XFEL beam in the vertical direction at HED (showing the shock was planar over the probed region) and $t = 0$ ns represents the time at which the drive laser was turned on.

Interaction Chamber 2 (IC2) at the HED instrument [82] of the EuXFEL during community campaign #6659. The second was conducted at the MEC end station [83] of the LCLS, during campaign L-1019923. A schematic of the standard experimental setup on HED is shown in Fig. 1. Pressure determination using the velocity interferometer system for any reflector (VISAR) [84–86] is described in Supplemental Material Sec. C [43].

A. Target design

We employed two sets of targets during the HED campaign: a windowed configuration of polyimide-Nb-lithium fluoride (LiF) (target A), and a free-surface polyimide-Nb (target B), as shown in Fig. 1(a). On the laser-drive side, for both targets types, a 50(2) μm-thick polyimide ablator was bonded with a 1.12(5) μm glue layer (Hardmann Double-Bubble epoxy) to an 18(2) μm-thick square of Nb foil (Goodfellow 99.9% purity). Individual component and combined target thicknesses were determined by averaging over point measurements made using a Heidenhain length gauge with 0.1 μm precision, enabling determination of the glue layer thickness. For the A-targets, which comprised approximately half of the targets used, a ∼150 μm-thick single-crystal (100)-LiF window, with a 400 nm Al flash-coating, was attached to the rear surface of the Nb foil for pressure determination using impedance matching. The flash-coated side of the LiF crystals was bonded to the Nb using another ∼micron layer of Hardmann Double-Bubble epoxy. Figure 1(b) shows a schematic of the experimental setup at HED.

B. Drive laser

Experiments at HED used the DiPOLE 100-X laser, an all-diode pumped 100 J-class ytterbium:YAG based laser with a frequency-doubled wavelength of 515 nm and a maximum repetition rate of 10 Hz [80,81]. However, during this experiment the laser was run at ∼0.02 Hz. The setup comprised a 250 μm phase plate, and the laser energy-polyimide pressure calibration was determined from polyimide-LiF shots preexperiment (Supplemental Material Sec. B [43]). Targets were driven using 10 ns quasi-flat-topped (125 ps rise time [87]) pulse shape, and a range of pulse energies from 4 to 49.5 J, to access single-shock states along the principal Hugoniot. Reproducible flat-top drive laser profiles and steady-state VISAR images after breakout revealed that the shock wave was temporally steady in the data presented here (shown in Supplemental Material Sec. K [43]).

At MEC, a Nd:glass optical laser, frequency doubled to a wavelength of 527 nm, was used with a 300 μm phase plate to focus a 10 ns quasi-flat-topped pulse shape into the ablator [88]. For the MEC experiments, we employed the same target A sample configuration as at HED and collected five shots with 80%–100% of the maximum available laser energy (100 J), thereby obtaining solid-liquid coexistence and liquid-only XRD data. At both facilities, the time delay between the laser drive and x-ray probe was tuned in each shot to ensure that the XRD data were obtained before shock breakout and release from the rear target surface.

C. VISAR diagnostics

At HED, three VISAR channels were used to monitor the shock arrival time. An example image from one of the channels is shown in Fig. 1(c). The pressure was determined from VISAR-recorded particle velocities by matching VISAR fringe jumps for targets with a LiF window at the Nb-LiF interface of type-A targets or free-surface breakout at the rear of type-B targets (Supplemental Material Sec. C [43]). The VISAR field of view was ∼650 μm but a smaller subset region (∼100 μm) was used to determine particle velocities (Supplemental Material Sec. C [43]). These channels operated at 532 and 1064 nm with varying velocity-per-fringe configurations to determine unique particle velocities solutions giving accurate measurements between 10 m/s to 100 km/s [86]. At MEC, two streak cameras operating at 532 nm were used to collect VISAR measurements perpendicular to the Nb-LiF interface. The field of view in this instance was ∼250 μm.

D. X-ray diffraction and density determination

At HED, a single pulse from the XFEL pulse train was delivered onto the sample with a focal spot size of 16 μm (V)×30 μm (H) (FWHM) at an angle of 22.5° to the target normal and VISAR axis [89]. The x-ray wavelength was 0.5166 Å and the sample to detector distance (SDD) was 317 mm. Two Varex large-area detectors [89], with a pixel size

of 150 μm × 150 μm, were employed to collect XRD images over a Q range of 1.5 to 14.3 Å^{-1} and azimuth range close to 180° [Fig. 1(b)], however, generally we were only able to resolve nonoverlapping shocked peaks up to 8.4 Å^{-1}. A CeO_2 standard placed at the sample position was used to refine the SDD and tilt of the detectors. The DIOPTAS [90] package was used to mask single crystal spots from LiF and integrate the XRD images into 1D profiles suitable for structure and density determination.

At MEC the x-ray beam was focused to 50 μm × 50 μm (FWHM) and centered on the focal spot of the drive laser which was aligned on the target. The x-ray wavelength was 0.7277 Å and the SDD was 687 mm. Similar to HED, Varex detectors were used at MEC spanning a Q range of 2.2 to 11.1 Å^{-1} allowing for high angle XRD coverage to be obtained up to the maximum angle. A CeO_2 standard was used for calibration, and XRD images were masked and integrated using the HEXRD [91] package.

All nonoverlapping diffraction peaks were fitted with Gaussians to determine their 2θ position. The density of the compressed Nb was then calculated using four to seven solid diffraction peaks per profile, depending on the pressure, and a Nb atomic mass of 92.906 amu [92]. Fewer peaks were used to determine the density of the compressed state compared to the ambient pattern due to (i) peak overlap, (ii) reduced intensity of broadened peaks resulting from area conservation at high strain rates, and (iii) additional intensity loss at elevated temperatures as a consequence of the Debye-Waller factor, especially at large Q [75]. Densities were corrected for variations in the SDD caused by manual mounting of targets and also the shot-to-shot x-ray beam jitter (see Supplemental Material Sec. F [43]).

III. RESULTS AND DISCUSSION

A. X-ray diffraction of niobium

An x-ray preshot was performed on each target prior to laser compression driven by flat-top drive laser profiles. In all reported data, the XFEL pulses probed the sample during shock transit (before shock breakout), thereby ensuring that XRD data were collected from only shock compressed volume and ambient (uncompressed) Nb in front of the shock. Figure 2 shows a waterfall plot of the 1D integrated diffraction profiles for selected runs collected at HED and MEC up to a Q of 8 Å^{-1}. In preshot profiles, up to 13 diffraction peaks from bcc-Nb were visible, from which the ambient lattice parameter was determined to be $a = 3.3021(5)$ Å from HED and $a = 3.3040(5)$ Å from MEC, consistent with previous work [11].

Diffraction peaks from the uncompressed Nb ahead of the shock wave were observed in all runs presented here, as seen in Fig. 2. The diffraction peaks from the compressed material are observed to shift towards greater Q with increasing pressure, as expected. Diffraction peaks from compressed Nb are significantly broader than those from uncompressed material due to large shock-induced strains [93,94] and variations in pressure states within large x-ray spot sizes [95]. In our experiment, these variations are expected to be smaller than the previously reported ∼2%−3% differences for a 50 μm × 50 μm XFEL x-ray spot with a 50 μm-thick polyimide ablator

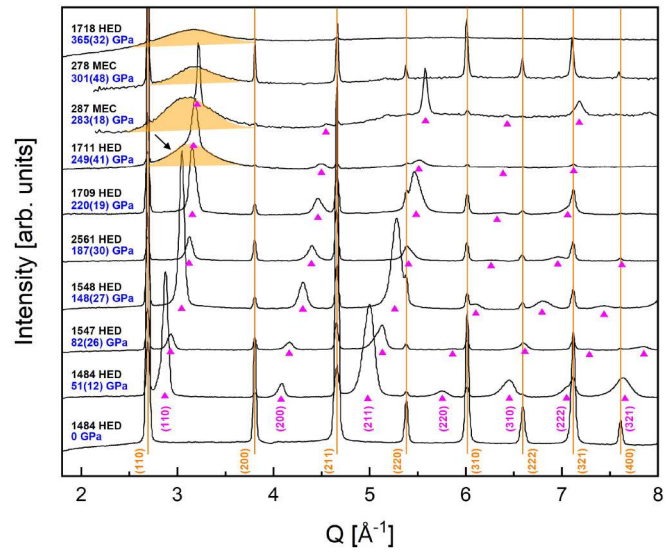


FIG. 2. Waterfall plot of the background subtracted integrated 1D XRD profiles from seven shots at HED and two at MEC. An ambient profile from Run 1484 HED is also shown. The pressure increases from bottom (0 GPa) to top (365 GPa). The black arrow highlights melting at P = 249(41) GPa (Run 1711 HED), as evident from the appearance of a diffuse scattering signal from the liquid phase. Shaded orange areas show a Gaussian peak, indicating the diffuse liquid scattering arising from the presence of melt. The sample was fully in the liquid state at 301(48) GPa. In each profile, ambient bcc-Nb peaks are identified by the orange lines while compressed-Nb peaks, if present, are identified by the pink triangles.

[95], due to employing a smaller x-ray probe at EuXFEL. We identify the onset of melting from the simultaneous weakening of bcc Bragg peaks and the emergence of liquidlike diffuse scattering around the (*110*) reflection, as can be seen at 249(41) GPa (Run 1711 HED) in the profile in Fig. 2. In other materials, such diffuse scattering has been reported as evidence of the liquid state [96–100]. Diffraction peaks from solid compressed Nb were not observed beyond 301 GPa (Run 278 at MEC—see Fig. 2), indicating that the sample is fully melted at this pressure. We obtained two shots in which the shocked Nb was fully molten, while weak peaks from uncompressed Nb remained from regions of the target ahead of the shock front confirming that the liquid signal arises from compressed material rather than a second stable solid phase at high pressure. The crystalline peaks in the liquid shots were confirmed to originate from ambient material, given the shock front transit time.

B. Structure of niobium along the principal Hugoniot

Figure 2 shows that shocked Nb remains stable in the bcc crystal structure along the Hugoniot up to the liquid state. The background-subtracted 1D integrated profile of shock-compressed Nb at 220(19) GPa (Run 1709 HED), the highest-pressure datum obtained before the onset of melting, can be seen in Fig. 3.

A Le Bail fit [101] to the 220 GPa profile (Fig. 3) shows that both compressed and uncompressed material have the bcc structure, with lattice parameters of 2.814(11) and

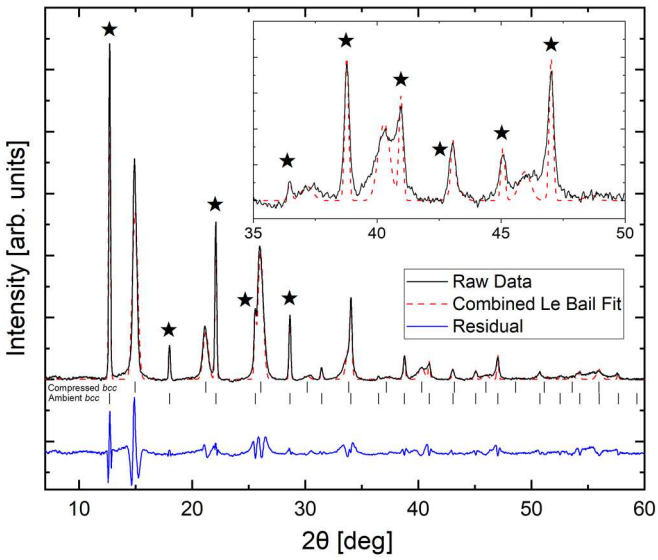


FIG. 3. The background-subtracted 1D diffraction profile from shocked-Nb at 220(19) GPa (Run 1709 HED). Stars have been added to highlight a number of low-angle peaks from uncompressed material. A two-phase Le Bail fit to the profile is shown as a red dashed line, confirming that the compressed material has the same bcc structure as that of Nb at ambient conditions. The residual to the fit is plotted as the blue line beneath the profile, and the insert provides an enlarged view of 35° to 50° range in 2θ.

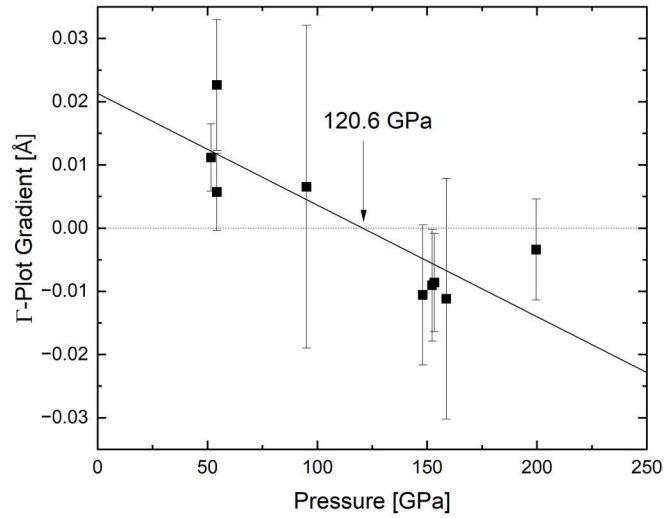


FIG. 4. The gradient of the Γ-plots as a function of pressure is shown for shots in which the d-spacings of the first five Bragg reflections could be measured. The gradient changes sign at 120.6 GPa, as a result of the change of sign of S, provided a positive t value.

3.3017(4) Å, respectively. At higher pressures, in the solid-liquid coexistence profiles obtained along the melt curve, we also see diffraction from compressed bcc-Nb in addition to scattering from the liquid (Fig. 2). We observe no evidence of the previously predicted bcc → hcp (∼75 GPa) or bcc → *Pnma* (∼142 GPa) phase changes in Nb along the principal Hugoniot [23,42,68]. Simulated profiles from the hcp and *Pnma* structures at 95 and 148 GPa, respectively, show that neither can explain the observed diffraction profiles at these pressures (Fig. S5). Furthermore, none of the *additional* diffraction peaks predicted by these structures is observed, enabling us to rule out the presence of both, even as a minority phase, above a volume fraction of 1.5%. The bcc crystal structure of Nb presented here along the principal Hugoniot is consistent with previous static compression studies up to 145 GPa [6,11–14].

C. Strength analysis

We found that the standard deviations in lattice parameters determined from the positions of individual XRD peaks within a given profile typically differed by 0.005 Å, and in one instance by up to 0.012 Å. This suggests the presence of residual elastic shear strain (i.e., strength) [93]. Variations of this magnitude are consistent with those expected in laser-driven shock compression experiments [93,94,102,103]. However, attempts to quantify the deviatoric stresses using the analysis of Singh and co-workers [104–106] were unsuccessful due to limited detector coverage and significant texture making it difficult to extract strain vs azimuth data around the Debye-Scherrer (DS) rings. Hence, we employed Singh's analysis using Γ-plots to determine the macroscopic deviatoric stress (t) along the principal Hugoniot (see Supplemental Material Sec. G [43]). Singh's method becomes unstable near 130 GPa for Nb, where small and rapidly changing values of the elastic anisotropy, $S = S_{11} - S_{12} - (S_{44}/2)$, (see Fig. S9) can lead to large, unphysical values of t. As a result, we were unable to extract meaningful information to quantify the macroscopic deviatoric stress. However, Fig. 4 shows the gradient in the linear fits of the Γ-plots changes sign at 120.6 GPa, as expected for a change in sign of S (assuming t remains positive). This estimated crossing pressure is in good agreement with the 130 GPa predicted from the elastic constants calculations of Wang *et al.* [107]. Our Singh analysis therefore provides experimental evidence for a sign change in S at 120.6 GPa, and consequently for the transition from heat-induced hardening to heat-induced softening described by Wang *et al.* [107], provided $dC_{44}/dP \gtrsim 0.28$. Wang *et al.* report a value of $dC_{44}/dP = 0.88$ along the principal Hugoniot.

D. Comparison to previous studies

The resulting pressure-density curve for shock-compressed Nb is shown in Fig. 5. The pressure-density Hugoniot behavior we observe in this work is consistent with previous shock compression studies on Nb in the solid phase up to 249 GPa along the principal Hugoniot [25,26,67,108–110]. Using static compression and laser-heating techniques, Errandonea *et al.* [23] reported a phase transition from cubic-bcc to orthorhombic-*Pnma* and predicted this transition to also occur along the principal Hugoniot. We do not observe any departure from the ambient-pressure bcc structure under our experimental conditions in the solid and solid-liquid coexistence regions along the principal Hugoniot. Kinetic effects due to the compression rate have previously been shown to influence structural transformations and can shift, or completely eliminate, phase transition boundaries in metals under dynamic vs static compression [97,111–113]. However, another possible solution is that under extended heating, Errandonea

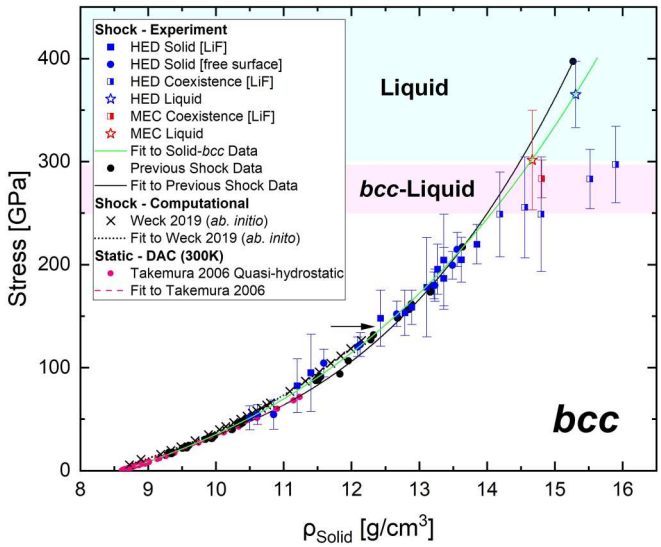


FIG. 5. The compression curve of bcc-Nb along the principal Hugoniot from data collected at HED (blue symbols) and MEC (red symbols). The green curve shows the fit to all our solid data, extrapolated to 365 GPa. The half filled squares indicate bcc-liquid coexistence and the two unfilled stars indicate fully molten Nb. For the two liquid shots the density was estimated from the extrapolated solid Hugoniot. The black crosses show the data obtained from the molecular dynamics simulations of Weck *et al.* [118], while the filled black circles show previous shock compression data [25,26,42,67,108–110]. The quasihydrostatic static compression data from Takemura *et al.* [11] at 300 K are shown as pink circles. The horizontal black arrow at 142 GPa identifies the predicted solid-solid phase transition pressure to *Pnma*-Nb from Errandonea *et al.* [23]. The pink shading shows the minimum bound for the bcc-liquid coexistence region, which starts at 249 GPa and ends at 298 GPa, while the blue shading shows the liquid region above 301 GPa, the pressure at which the fully melted Nb was first observed at MEC. The average error on the pressure and density is 25 GPa and 0.02 g/cm^3 respectively for our data from HED and MEC.

et al. formed a Nb-carbide due to carbon diffusion from the diamond anvils. Their published results show no evidence that a single phase, *Pnma*-only, diffraction profile was obtained, perhaps suggesting partial reaction of the sample. Although *Pnma* symmetry has been reported in Nb_2C [114–116], its lattice parameters are different to those reported by Errandonea *et al.* However, the Z-method used by Errandonea *et al.* has previously been shown to struggle to resolve temperature induced solid-solid transitions [117], while the recent *ab initio* calculations by Wang *et al.* [107] have shown the proposed high-T *Pnma* structure to be mechanically unstable under hydrostatic conditions. Repeating the calculations of Errandonea *et al.* resulted in significant stress anisotropy, suggesting that the *Pnma* structure may only achieve metastability under non-hydrostatic conditions [107].

Al'tshuler *et al.* [42] interpreted a change in the U_s-U_p slope at 94 GPa as a second-order phase transition. Scatter in our U_s-U_p data makes it unclear whether such a slope change is observed in this study (Supplemental Material Sec. D [43]). We find limited evidence for this transition, with no anomalies observed along the compression curve in Fig. 5.

Incipient melting of Nb was observed to start at 249(41) GPa (Run 1711 HED) and was complete at 301(48) GPa (Run 278 MEC), Fig. 2. Recent *ab initio* calculations by Wang *et al.* [107] reported melting of Nb to begin at 207 GPa (6850 K) and reach the liquid state at 255 GPa (7400 K), around 50 GPa lower than the experimental values presented here. Therefore, our data suggest a steeper melt curve than previous studies [23,107,119]. We observed profiles of molten Nb at 301(48) GPa at MEC and 365(32) GPa at HED. As no density for liquid-Nb was determined, the liquid data points (unfilled stars in Fig. 5) have been plotted using densities estimated from the extrapolated solid Hugoniot and pressures determined from VISAR.

Within the solid-liquid coexistence region, we obtained five shots at HED, and one at MEC. Interestingly, around the melt transition the VISAR velocities increase weakly with increasing drive laser power, while the density of the solid component continues to increase significantly. This leads to an apparent softening away from the extrapolated solid Hugoniot (green curve) in Fig. 5.

We attribute the deviation observed in the pink-shaded coexistence region of Fig. 5 to the following. For phase boundaries with a positive Clapeyron slope [120], such as in Fe [99], the solid phase is denser than the coexisting liquid at a given (P, T). Consequently, densities determined from the solid component are expected to lie at higher density than the bulk equation of state (represented by the linear U_s-U_p model, which should not differ to a large extent in the incipient melting regime from that established in the solid regime). Within the coexistence region, the Hugoniot density corresponds to a volume-fraction-weighted average of the coexisting solid and liquid densities. The solid densities shown in Fig. 5 (half filled squares) therefore lie on the solidus, rather than on the Hugoniot, hence their increased density relative to the extrapolated solid Hugoniot (green curve), while remaining on the melt curve.

IV. CONCLUSION

In conclusion, through a combination of experiments using the DiPOLE 100-X laser at the HED instrument of the EuXFEL and the long-pulse laser at the MEC end station of the LCLS, we have shock compressed Nb along the principal Hugoniot and observed the persistence of the low-pressure bcc structure up to 220 GPa before the onset of melting. By combining multiple shots carried out at both facilities, we present XRD data from 51 GPa (bcc) to 365 GPa (liquid). We find that the principal Hugoniot starts to intersect the Nb melt curve at 249 GPa, and the transition to the pure liquid phase is complete at 301 GPa, suggesting a steeper melt curve than previously predicted. Based on our *in situ* XRD measurements, we do not observe any previously reported phase transitions and Nb remains stable in the bcc structure up to liquid.

ACKNOWLEDGMENTS

UK Ministry of Defence © Crown owned copyright 2026/AWE. Experimental results were obtained during

collaborative proposal #6659, carried out in November 2024 at EuXFEL (Main Proposer: Guillaume Morard; Principal Investigator: Jon Eggert; Local Contact: Karen Appel), with the assistance of pillar leaders Adrien Descamps, Andrew Higginbotham, Trevor Hutchinson, Chris McGuire, Silvia Pandolfi and Arnaud Sollier. C.M.L. thanks M.G. Gorman for his help and advice with this project. We acknowledge the European XFEL in Schenefeld, Germany, for provision of x-ray free electron laser beam time at the Scientific Instrument HED (High Energy Density Science) and would like to thank the staff for their assistance. The authors are indebted to the Helmholtz International Beamline for Extreme Fields (HIBEF) user consortium for the provision of instrumentation and staff that enabled this experiment. Use of the Linac Coherent Light Source (LCLS) SLAC National Accelerator Laboratory, is supported by the U.S. Department of Energy Office of Science (SC), Basic Energy Science under Contract No. DE-AC02-76SF00515. This research was supported by SC, Fusion Energy Science, FWP 100106: The LaserNetUS Initiative at Matter in Extreme Conditions, under Contract No. DE-AC02-76SF00515. C.M.L. and C.R.R. are grateful to S.G. MacLeod and AWE for the award of their studentships (No. WT13356629 and No. WT14175294). This work was supported by Grants No. EP/S022155/1 (J.D.M., C.V.S., M.I.M.), No. EP/Z533671/1 (J.D.M., C.V.S., M.I.M.), No. EP/S023585/1 (A.H.), No. EP/X025373/1 (A.H.), No. EP/W010097/1 (C.C.), No. EP/X031624/1 (P.G.H.), No. EP/S022430/1 (A-M.N., J.D.U.-T.) and No. EP/X031624/1 (J.S.W.) from the UK Engineering and Physical Sciences Research Council (EPSRC). R.S.W. and N.J. acknowledge funding from the European Research Council (ERC) under the European Union's Horizon 2020 research and innovation programme (Grant Agreement No. 101002868). R.F.S., T.M.H., P.A., A.K., I.K.O., S.S., C.E.V., C.M., and J.H.E. acknowledge this work was performed in part under the auspices of the U.S. Department of Energy by Lawrence Livermore National Laboratory under contract DE-AC52-07NA27344, and was supported by the Laboratory Directed Research and Development Program at LLNL (Project No. 24-ERD-021). E.E.M. and A.D. were supported by the UK Research and Innovation Future Leaders Fellowship (MR/W008211/1) awarded to E.E.M. S.P. acknowledges support from the ANR grant HEX-DYN (ANR-24-CE30-4792). A.A. and N.O. acknowledge supports from Japan Society for the Promotion of Science (JSPS) KAKENHI (Grants No. 23K20038, No. 25H00618, and No. 22F22707), JSPS Core-to-Core Program (JPJSCCA20230003), and MEXT Quantum Leap Flagship Program (JPMXS0118067246). G.M., S.M., and A.C. received support from the Agence Nationale de la Recherche (ANR grant MIN-DIXI, ANR-22-CE49-0006). K.A. and K.B. acknowledge financial support by the Deutsche Forschungsgemeinschaft (DFG, German Research Foundation) via project AP262/2-2 (Project No. 280637173). K.A. and C.C. acknowledge funding by the Deutsche Forschungsgemeinschaft (DFG, German Research Foundation) via project AP262/3-1 (Project No. 521549147) under Germany's Priority Programme "Reconstructing the deep dynamics of planet Earth over geologic time (DeepDyn) SPP2404–500707704. This research is supported by the European Union: S.M., J.C., and H.G. (ERC, HotCores, Grant No. 101054994), D.K. (ERC, MEGACHEM, Grant No. 101171289). Views and opinions expressed are however those of the author(s) only and do not necessarily reflect those of the European Union or the European Research Council. Neither the European Union nor the granting authority can be held responsible for them. G.W.C. and T.-A.S. acknowledge this material is based upon work supported by the Department of Energy [National Nuclear Security Administration] University of Rochester "National Inertial Confinement Fusion Program" under Award No. DE-NA0004144. This work was supported by the Center for Matter at Atomic Pressures (CMAP), a National Science Foundation (NSF) Physics Frontiers Center, under Award PHY2020249. Y.D., X.F., S.-N.L., M.T., and L.W. acknowledge this work was partially supported by the National Natural Science Foundation of China (Grant No. 12402466, 11627901). L.D.M., S.E.P., and A.H. were supported by the Department of Energy—National Nuclear Security Administration Center of Excellence CAMCSE under Award No. DE-NA0004154. S.G., F.H., I.I.O., C.N.S., and A.T. acknowledge the work at USF is supported by DOE/NNSA (Awards No. DE-NA-0004089 and No. DE-NA0004234), DOE/FES (Award No. DE-SC0024640), Lawrence Livermore National Laboratory's Academic Collaborative Team (ACT) award, NSF (Award No. 2421937), and NASA (Award No. 80NSSC25K7172). N.J.H. was supported by the DOE Office of Science, Fusion Energy Science under FWP 100182. J.-A.H. was supported by the European Synchrotron Radiation Facility. J.K. acknowledges the National Research Foundation of Korea (RS-2024-00416036). The work of D.K. was supported by Deutsche Forschungsgemeinschaft (DFG—German Research Foundation) Project No. 505630685. C.O. and C.P. acknowledge support by the German Federal Ministry of Education and Research (BMBF) under grant 05K22VF1 within the ExtremeLight project. D.J.P. and T.S. appreciate support from AWE via the Oxford Centre for High Energy Density Science (OxCHEDS). D.R. was supported by STFC Grant No. R1153APL. L.R. acknowledges funding from the National Science Center, Poland, under Grant No. 2021/41/B/ST8/03758. U.T. acknowledges the financial support from the Slovenian Research and Innovation Agency (ARIS) research core funding No. P2-0270 and ARIS research Project No. J2-60033 (SuperShocked). Additionally, the authors would like to thank the Horizon Europe framework's Sustainable Blue Economy Partnership for funding the CORRASBlue project.

C.M.L. led the original draft preparation with support from J.D.M., C.V.S. and M.I.M. C.M.L. carried out the formal analysis with support from J.D.M., C.V.S., R.S.M., M.J. and R.F.S. J.D.M. conceptualized the experiment with support from C.M.L., C.V.S., M.I.M., R.S.M., R.F.S., A.D., A.H., T.M.H., S.P., A.S., C.M., G.M. and J.H.E. M.I.M, A.D., A.H., T.M.H., S.P., A.S., C.M., G.M. and J.H.E. supervised the project. A.D., A.H., T.M.H., S.P., A.S., C.M., G.M. and J.H.E. carried out project administration. M.I.M., G.M. and J.H.E. secured funding. K.A. lead facility support with assistance from M.A., E.B., K.B., S.D.D.D.C., C.C., E.G., D.K., Z.K., H.J.L., T.M., M.N., T.R.P. and M.X.T. C.M.L., J.D.M., C.V.S., M.I.M., R.S.M., N.J., R.F.S., A.D., A.H., T.M.H., S.P., A.S., M.A., K.A., P.A., E.B., N.B., K.B., S.D.D.D.C., C.C., O.C., A.C., J.C., D.M.C., A.J.C., C.C., Y.D., X.F., M.D.F.,

E.G., H.G., A.H., M.H., P.G.H., H.H., D.K., J.K., Z.K., D.K., H.J.L., D.M., S.M., T.M., M.N., A-M.N., I.O., I.I.O., S.E.P., D.J.P., A.P., T.R.P., N.P., L.R., J-P.S., G.S., S.S., C.S., M.X.T., T.T., U.T., J.D.U.-T., C.E.V., C.M., G.M. and J.H.E. contributed equally to the experimental investigation. All authors contributed equally to the experimental methodology and the final editing of the manuscript.

DATA AVAILABILITY

The data is available upon reasonable request at Ref. [121].

[1] E. P. George, D. Raabe, and R. O. Ritchie, High-entropy alloys, Nat. Rev. Mater. **4**, 515 (2019).

[2] M. Feuerbacher, T. Lienig, and C. Thomas, A single-phase bcc high-entropy alloy in the refractory Zr-Nb-Ti-V-Hf system, Scr. Mater. **152**, 40 (2018).

[3] J. E. Williams, Superconducting magnets and their applications, Proc. IEEE **77**, 1132 (2002).

[4] Q. Deng, Y. Fu, C. Zhu, and Y. Yu, Niobium-based oxides toward advanced electrochemical energy storage: Recent advances and challenges, Small **15**, 1804884 (2019).

[5] L. Yan, X. Rui, G. Chen, W. Xu, G. Zou, and H. Luo, Recent advances in nanostructured Nb-based oxides for electrochemical energy storage, Nanoscale **8**, 8443 (2016).

[6] Q. M. Jing, Q. He, Y. Zhang, S. R. Li, L. Liu, Q. Y. Hou, H. Y. Geng, Y. Bi, Y. Y. Yu, and Q. Wu, Unusual softening behavior of yield strength in niobium at high pressures, Chin. Phys. B **27**, 106201 (2018).

[7] L. Koči, Y. Ma, A. R. Oganov, P. Souvatzis, and R. Ahuja, Elasticity of the superconducting metals V, Nb, Ta, Mo, and W at high pressure, Phys. Rev. B **77**, 214101 (2008).

[8] A. Landa, J. Klepeis, P. Söderlind, I. Naumov, O. Velikokhatnyi, L. Vitos, and A. Ruban, *Ab initio* calculations of elastic constants of the bcc V-Nb system at high pressures, J. Phys. Chem. Solids **67**, 2056 (2006).

[9] Y. X. Wang, H. Y. Geng, Q. Wu, X. R. Chen, and Y. Sun, First-principles investigation of elastic anomalies in niobium at high pressure and temperature, J. Appl. Phys. **122**, 235903 (2017).

[10] A. K. Singh and T. Kenichi, Measurement and analysis of nonhydrostatic lattice strain component in niobium to 145 GPa under various fluid pressure-transmitting media, J. Appl. Phys. **90**, 3269 (2001).

[11] T. Kenichi and A. K. Singh, High-pressure equation of state for Nb with a helium-pressure medium: Powder x-ray diffraction experiments, Phys. Rev. B **73**, 224119 (2006).

[12] A. K. Singh and H. P. Liermann, Strength and elasticity of niobium under high pressure, J. Appl. Phys. **109**, 113539 (2011).

[13] A. K. Singh and H. P. Liermann, Strength of polycrystalline niobium from high-pressure x-ray diffraction data: A comparison of results from line-width and line-shift analyses, J. Appl. Phys. **118**, 065903 (2015).

[14] A. K. Singh and K. Takemura, Negative differential stresses in niobium: Analysis of x-ray measured pressure-volume data, J. Appl. Phys. **128**, 075901 (2020).

[15] M. Masoumi, B. R. Saraiva, P. W. Sarvezuk, L. Novotný, T. C. Andrade, H. F. de Abreu, and M. Béreš, Pressure-induced tetragonal distortion in niobium: Insights from synchrotron X-ray diffraction, Mater. Today Commun. **44**, 111948 (2025).

[16] Y. X. Wang, H. Y. Geng, Q. Wu, and X. R. Chen, Orbital localization error of density functional theory in shear properties of vanadium and niobium, J. Chem. Phys. **152**, 024118 (2020).

[17] S. P. Kramynin and E. N. Akhmedov, Equation of state and properties of Nb at high temperature and pressure, J. Phys. Chem. Solids **135**, 109108 (2019).

[18] Y. Wang, H. Wu, Y. Liu, H. Wang, X. Chen, and H. Geng, Recent progress in phase stability and elastic anomalies of group VB transition metals, Crystals **12**, 1762 (2022).

[19] H. Oli, B. Acharya, and N. P. Adhikari, First-principles study of superconducting transition temperature of niobium and vanadium as a function of pressure, AIP Adv. **14**, 045246 (2024).

[20] D. Goldberg, G. Dicker, and S. Worcester, Niobium and niobium alloys in nuclear power, Nucl. Eng. Des. **22**, 124 (1972).

[21] K. A. Gschneidner Jr, Physical properties and interrelationships of metallic and semimetallic elements, in *Solid State Physics* (Elsevier, Amsterdam, 1964), Vol. 16, pp. 275–426.

[22] D. R. Lide, *CRC Handbook of Chemistry and Physics* (CRC Press, Boca Raton, FL, 2004), Vol. 85.

[23] D. Errandonea, L. Burakovsky, D. L. Preston, S. G. MacLeod, D. Santamaría-Perez, S. Chen, H. Cynn, S. I. Simak, M. I. McMahon, J. E. Proctor, *et al.*, Experimental and theoretical confirmation of an orthorhombic phase transition in niobium at high pressure and temperature, Commun. Mater. **1**, 60 (2020).

[24] D. Errandonea, B. Schwager, R. Ditz, C. Gessmann, R. Boehler, and M. Ross, Systematics of transition-metal melting, Phys. Rev. B **63**, 132104 (2001).

[25] R. McQueen, S. Marsh, J. Taylor, J. Fritz, and W. Carter, The equation of state of solids from shock wave studies, High Velocity Impact Phenom., 293 (1970).

[26] S. P. Marsh, *LASL Shock Hugoniot Data* (University of California Press, California, 1980), Vol. 5.

[27] D. Errandonea, S. MacLeod, L. Burakovsky, D. Santamaria-Perez, J. Proctor, H. Cynn, and M. Mezouar, Melting curve and phase diagram of vanadium under high-pressure and high-temperature conditions, Phys. Rev. B **100**, 094111 (2019).

[28] M. Stevenson, E. Pace, C. Storm, S. Finnegan, G. Garbarino, C. Wilson, D. McGonegle, S. Macleod, and M. McMahon, Pressure-induced bcc-rhombohedral phase transition in vanadium metal, Phys. Rev. B **103**, 134103 (2021).

[29] X. Huang, F. Li, Q. Zhou, Y. Meng, K. D. Litasov, X. Wang, B. Liu, and T. Cui, Thermal equation of state of molybdenum determined from *in situ* synchrotron x-ray diffraction with laser-heated diamond anvil cells, Sci. Rep. **6**, 19923 (2016).

[30] K. D. Litasov, P. I. Dorogokupets, E. Ohtani, Y. Fei, A. Shatskiy, I. S. Sharygin, P. N. Gavryushkin, S. V. Rashchenko, Y. V. Seryotkin, Y. Higo, *et al.*, Thermal equation of state and thermodynamic properties of molybdenum at high pressures, J. Appl. Phys. **113**, 093507 (2013).

[31] R. Hixson and J. Fritz, Shock compression of tungsten and molybdenum, J. Appl. Phys. **71**, 1721 (1992).

[32] J. Wang, F. Coppari, R. F. Smith, J. H. Eggert, A. E. Lazicki, D. E. Fratanduono, J. R. Rygg, T. R. Boehly, G. W. Collins, and T. S. Duffy, X-ray diffraction of molybdenum under shock compression to 450 GPa, Phys. Rev. B **92**, 174114 (2015).

[33] J. Wang, F. Coppari, R. F. Smith, J. H. Eggert, A. E. Lazicki, D. E. Fratanduono, J. R. Rygg, T. R. Boehly, G. W. Collins, and T. S. Duffy, X-ray diffraction of molybdenum under ramp compression to 1 TPa, Phys. Rev. B **94**, 104102 (2016).

[34] J. Brown and J. Shaner, Rarefaction velocities in shocked tantalum and the high pressure melting point, in *Shock Waves in Condensed Matter 1983* (Elsevier, Amsterdam, 1984), pp. 91–94.

[35] A. Dewaele, M. Mezouar, N. Guignot, and P. Loubeyre, High melting points of tantalum in a laser-heated diamond anvil cell, Phys. Rev. Lett. **104**, 255701 (2010).

[36] M. Gorman, C. Wu, R. Smith, L. Benedict, C. Prisbrey, W. Schill, S. Bonev, Z. Long, P. Söderlind, D. Braun, *et al.*, Ramp compression of tantalum to multiterapascal pressures: Constraints of the thermal equation of state to 2.3 TPa and 5000 K, Phys. Rev. B **107**, 014109 (2023).

[37] J. Eggert, R. Smith, D. Swift, R. Rudd, D. Fratanduono, D. Braun, J. Hawreliak, J. McNaney, and G. Collins, Ramp compression of tantalum to 330 GPa, High Press. Res. **35**, 339 (2015).

[38] D. Errandonea, M. Somayazulu, D. Häusermann, and H. Mao, Melting of tantalum at high pressure determined by angle dispersive x-ray diffraction in adouble-sided laser-heated diamond-anvil cell, J. Phys.: Condens. Matter **15**, 7635 (2003).

[39] R. Kraus, F. Coppari, D. Fratanduono, R. Smith, A. Lazicki, C. Wehrenberg, J. Eggert, J. Rygg, and G. Collins, Melting of tantalum at multimegabar pressures on the nanosecond timescale, Phys. Rev. Lett. **126**, 255701 (2021).

[40] R. Trunin, A. Medvedev, A. Funtikov, M. Podurets, G. Simakov, and A. Sevast'yanov, Shock compression of porous iron, copper and tungsten: And their equation of state in the terapascal pressure range, Sov. Phys. JETP **68**, 356 (1989).

[41] L. Dubrovinsky and S. Saxena, Thermal expansion of periclase (MgO) and tungsten (W) to melting temperatures, Phys. Chem. Miner. **24**, 547 (1997).

[42] L. Al'tshuler, A. Bakahova, and I. Dudoladov, Effect of electron structure on the compressibility of metals at high pressure, Sov. Phys. JETP **26**, 1115 (1968).

[43] See Supplemental Material at http://link.aps.org/supplemental/10.1103/tlxw-bfx4 for a complete set of experimental data collected and analysis techniques used in this paper, which includes Refs. [44–66].

[44] P. Celliers, G. Collins, D. Hicks, and J. Eggert, Systematic uncertainties in shock-wave impedance-match analysis and the high-pressure equation of state of Al, J. Appl. Phys. **98**, 113529 (2005).

[45] T. Vinci, NeutrinoToolkit/Neutrino: Image analysis for plasma physics, https://github.com/NeutrinoToolkit/Neutrino (2024).

[46] P. Simpkins, Physics of shock waves and high-temperature hydrodynamic phenomena. Zel'dovich and Raizer. Academic Press, New York and London. 1966. 464 pp. 144s, Aeron. J. **71**, 731 (1967).

[47] J. M. Walsh and R. H. Christian, Equation of state of metals from shock wave measurements, Phys. Rev. **97**, 1544 (1955).

[48] A. Benuzzi-Mounaix, M. Koenig, G. Huser, B. Faral, D. Batani, E. Henry, M. Tomasini, B. Marchet, T. Hall, M. Boustie, *et al.*, Absolute equation of state measurements of iron using laser driven shocks, Phys. Plasmas **9**, 2466 (2002).

[49] L. Al'Tshuler, K. Krupnikov, B. Ledenev, V. Zhuchikhin, and M. Brazhnik, Dynamic compressibility and equation of state of iron under high pressure, Sov. Phys. JETP **34** (1958).

[50] L. Al'Tshuler, S. Kormer, A. Bakanova, and R. Trunin, Equation of state for aluminum, copper, and lead in the high pressure region, Sov. Phys. JETP **11**, 573 (1960).

[51] Z. Yan, H. Liu, X. Zhang, G. Ren, J. Liu, W. Kang, W. Zhang, and X. He, Dynamics of particles near the surface of a medium under ultra-strong shocks, Matter Radiat. Extremes **6**, 026903 (2021).

[52] N. Nissim, E. Greenberg, M. Werdiger, Y. Horowitz, L. Bakshi, Y. Ferber, B. Glam, A. Fedotov-Gefen, L. Perelmutter, and S. Eliezer, Free-surface velocity measurements of opaque materials in laser-driven shock-wave experiments using photonic Doppler velocimetry, Matter Radiat. Extremes **6**, 046902 (2021).

[53] P. W. Cooper, *Explosives Engineering* (John Wiley & Sons, Hoboken, NJ, 1996).

[54] P. Rigg, M. Knudson, R. Scharff, and R. Hixson, Determining the refractive index of shocked [100] lithium fluoride to the limit of transmissibility, J. Appl. Phys. **116**, 033515 (2014).

[55] B. Jensen, D. Holtkamp, P. Rigg, and D. Dolan, Accuracy limits and window corrections for photon Doppler velocimetry, J. Appl. Phys. **101**, 013523 (2007).

[56] J. A. Hawreliak, J. Winey, Y. Toyoda, M. Wallace, and Y. M. Gupta, Shock-induced melting of [100] lithium fluoride: Sound speed and Hugoniot measurements to 230 GPa, Phys. Rev. B **107**, 014104 (2023).

[57] K. Momma and F. Izumi, VESTA 3 for three-dimensional visualization of crystal, volumetric and morphology data, J. Appl. Cryst. **44**, 1272 (2011).

[58] A. K. Singh, E. Menéndez-Proupin, G. Gutiérrez, Y. Akahama, and H. Kawamura, Nonhydrostatic compression of bismuth to 222 GPa: Some constraints on elasticity of the bcc-phase, J. Phys. Chem. Solids **67**, 2192 (2006).

[59] C. V. Storm, G. A. Woolman, C. M. Lonsdale, J. D. McHardy, M. J. Duff, G. J. Ackland, and M. I. McMahon, Experimental and computational study of the core-level crossing transition in iridium at high pressure, Phys. Rev. B **109**, 024101 (2024).

[60] C. V. Storm, J. D. McHardy, M. J. Duff, S. G. MacLeod, E. F. O'Bannon III, and M. I. McMahon, The stress state in bismuth to 298 GPa and its use as a pressure transmitting medium and pressure marker at multi-megabar pressures, J. Appl. Phys. **133**, 245904 (2023).

[61] D. J. Campbell, D. T. Sneed, E. F. O'Bannon III, P. Söderlind, and Z. Jenei, Refined room-temperature equation of state of Bi up to 260 GPa, Phys. Rev. B **107**, 224104 (2023).

[62] N. Funamori, M. Funamori, R. Jeanloz, and N. Hamaya, Broadening of x-ray powder diffraction lines under nonhydrostatic stress, J. Appl. Phys. **82**, 142 (1997).

[63] C. M. Lonsdale, J. D. McHardy, C. V. Storm, K. Glazyrin, M. Mezouar, and M. I. McMahon, A closer look under extreme pressure: Sub-micron diffraction mapping in a diamond anvil cell, High Press. Res. **46**, 56 (2026).

[64] L. Lutterotti, R. Vasin, and H.-R. Wenk, Rietveld texture analysis from synchrotron diffraction images. I. Calibration and basic analysis, Powder Diffr. **29**, 76 (2014).

[65] H.-R. Wenk, L. Lutterotti, P. Kaercher, W. Kanitpanyacharoen, L. Miyagi, and R. Vasin, Rietveld texture analysis from synchrotron diffraction images. II. Complex multiphase materials and diamond anvil cell experiments, Powder Diffr. **29**, 220 (2014).

[66] W. B. Holzapfel, Equations of state for solids under strong compression, High Press. Res. **16**, 81 (1998).

[67] W. H. Isbell, F. H. Shipman, and A. H. Jones, Hugoniot equation of state measurements for eleven materials to five megabars, Report MSL-68-13 (General Motors Corporation, Materials Science Laboratory, 1968).

[68] T. C. Germann, Large-scale classical molecular dynamics simulations of shock-induced plasticity in bcc niobium, in *AIP Conference Proceedings* (American Institute of Physics, 2009), Vol. 1195, pp. 761–764.

[69] Y. Ding, R. Ahuja, J. Shu, P. Chow, W. Luo, and H.-K. Mao, Structural phase transition of vanadium at 69 GPa, Phys. Rev. Lett. **98**, 085502 (2007).

[70] R. Briggs, F. Coppari, M. Gorman, R. Smith, S. Tracy, A. Coleman, A. Fernandez-Pañella, M. Millot, J. Eggert, and D. Fratanduono, Measurement of body-centered cubic gold and melting under shock compression, Phys. Rev. Lett. **123**, 045701 (2019).

[71] M. Millot, F. Coppari, J. R. Rygg, A. Correa Barrios, S. Hamel, D. C. Swift, and J. H. Eggert, Nanosecond X-ray diffraction of shock-compressed superionic water ice, Nature (London) **569**, 251 (2019).

[72] M. Gorman, D. McGonegle, R. Smith, S. Singh, T. Jenkins, R. McWilliams, B. Albertazzi, S. Ali, L. Antonelli, M. Armstrong, *et al.*, Shock compression experiments using the DiPOLE 100-X laser on the high energy density instrument at the European x-ray free electron laser: Quantitative structural analysis of liquid Sn, J. Appl. Phys. **135**, 165902 (2024).

[73] A. L. Coleman, S. Singh, T. E. Lockard, I. K. Ocampo, A. E. Lazicki, M. G. Gorman, S. Racioppi, A. G. Krygier, C. E. Wehrenberg, R. Ahmad, *et al.*, Body-centered-cubic phase transformation in gold at TPa pressures, Phys. Rev. Lett. **135**, 186101 (2025).

[74] K. A. Pereira, S. M. Clarke, S. Singh, R. Briggs, C. P. McGuire, H. J. Lee, D. Khaghani, B. Nagler, E. Galtier, E. Cunningham, *et al.*, Stability of the fcc phase in shocked nickel up to 332 GPa, Nat. Commun. **16**, 4385 (2025).

[75] J. S. Wark, D. Peake, T. Stevens, P. Heighway, Y. Ping, P. Sterne, B. Albertazzi, S. Ali, L. Antonelli, M. Armstrong, *et al.*, Femtosecond temperature measurements of laser-shocked copper deduced from the intensity of the x-ray thermal diffuse scattering, J. Appl. Phys. **137**, 155904 (2025).

[76] A. Gleason, C. A. Bolme, H. J. Lee, B. Nagler, E. Galtier, D. Milathianaki, J. Hawreliak, R. Kraus, J. Eggert, D. Fratanduono, *et al.*, Ultrafast visualization of crystallization and grain growth in shock-compressed SiO_2, Nat. Commun. **6**, 8191 (2015).

[77] R. Briggs, M. Gorman, A. Coleman, R. McWilliams, E. McBride, D. McGonegle, J. Wark, L. Peacock, S. Rothman, S. Macleod, *et al.*, Ultrafast x-ray diffraction studies of the phase transitions and equation of state of scandium shock compressed to 82 GPa, Phys. Rev. Lett. **118**, 025501 (2017).

[78] A. Gleason, C. A. Bolme, E. Galtier, H. J. Lee, E. Granados, D. Dolan, C. Seagle, T. Ao, S. Ali, A. Lazicki, *et al.*, Compression freezing kinetics of water to ice VII, Phys. Rev. Lett. **119**, 025701 (2017).

[79] M. I. McMahon, Probing extreme states of matter using ultra-intense x-ray radiation, J. Phys.: Condens. Matter **34**, 043001 (2022).

[80] P. Mason, S. Banerjee, J. Smith, T. Butcher, J. Phillips, H. Höppner, D. Möller, K. Ertel, M. De Vido, I. Hollingham, *et al.*, Development of a 100 J, 10 Hz laser for compression experiments at the High Energy Density instrument at the European XFEL, High Power Laser Sci. Eng. **6**, e65 (2018).

[81] J. P. Phillips, S. Banerjee, P. Mason, J. Smith, J. Spear, M. De Vido, K. Ertel, T. Butcher, G. Quinn, D. Clarke, *et al.*, Second and third harmonic conversion of a kilowatt average power, 100-J-level diode pumped Yb: YAG laser in large aperture LBO, Opt. Lett. **46**, 1808 (2021).

[82] U. Zastrau, K. Appel, C. Baehtz, O. Baehr, L. Batchelor, A. Berghäuser, M. Banjafar, E. Brambrink, V. Cerantola, T. E. Cowan, *et al.*, The high energy density scientific instrument at the European XFEL, J. Synchrotron Radiat. **28**, 1393 (2021).

[83] B. Nagler, B. Arnold, G. Bouchard, R. F. Boyce, R. M. Boyce, A. Callen, M. Campell, R. Curiel, E. Galtier, J. Garofoli, *et al.*, The matter in extreme conditions instrument at the Linac Coherent Light Source, J. Synchrotron Rad. **22**, 520 (2015).

[84] L. M. Barker and R. Hollenbach, Shock-wave studies of PMMA, fused silica, and sapphire, J. Appl. Phys. **41**, 4208 (1970).

[85] L. Barker and R. Hollenbach, Laser interferometer for measuring high velocities of any reflecting surface, J. Appl. Phys. **43**, 4669 (1972).

[86] A. Descamps, T. M. Hutchinson, R. Briggs, E. E. McBride, M. Millot, T. Michelat, J. H. Eggert, B. Albertazzi, L. Antonelli, M. R. Armstrong, *et al.*, Calibration and characterization of the line-VISAR diagnostic at the HED-HIBEF instrument at the European XFEL, Rev. Sci. Instrum. **96**, 075206 (2025).

[87] V. Cerantola, A. D. Rosa, Z. Konôpková, R. Torchio, E. Brambrink, A. Rack, U. Zastrau, and S. Pascarelli, New frontiers in extreme conditions science at synchrotrons and free electron lasers, J. Phys.: Condens. Matter **33**, 274003 (2021).

[88] S. H. Glenzer, L. B. Fletcher, E. Galtier, B. Nagler, R. Alonso-Mori, B. Barbrel, S. B. Brown, D. A. Chapman, Z. Chen, C. B. Curry, *et al.*, Matter under extreme conditions experiments at the Linac coherent light source, J. Phys. B: At. Mol. Opt. Phys. **49**, 092001 (2016).

[89] H.-P. Liermann, Z. Konôpková, K. Appel, C. Prescher, A. Schropp, V. Cerantola, R. Husband, J. McHardy, M. McMahon, R. McWilliams, *et al.*, Novel experimental setup for megahertz X-ray diffraction in a diamond anvil cell at the High Energy Density (HED) instrument of the European X-ray Free-Electron Laser (EuXFEL), J. Synchrotron Rad. **28**, 688 (2021).

[90] C. Prescher and V. B. Prakapenka, DIOPTAS: A program for reduction of two-dimensional X-ray diffraction data and data exploration, High Press. Res. **35**, 223 (2015).

[91] D. E. Boyce and J. V. Bernier, heXRD: Modular, open source software for the analysis of high energy X-ray diffraction data, Technical Report (Lawrence Livermore National Lab. (LLNL), Livermore, CA, 2013).

[92] T. Prohaska, J. Irrgeher, J. Benefield, J. K. Böhlke, L. A. Chesson, T. B. Coplen, T. Ding, P. J. Dunn, M. Gröning, N. E.

Holden, *et al.*, Standard atomic weights of the elements 2021 (IUPAC technical report), Pure Appl. Chem. **94**, 573 (2022).

[93] A. Higginbotham and D. McGonegle, Prediction of Debye-Scherrer diffraction patterns in arbitrarily strained samples, J. Appl. Phys. **115**, 174906 (2014).

[94] S. Pandolfi, S. B. Brown, P. Stubley, A. Higginbotham, C. Bolme, H. Lee, B. Nagler, E. Galtier, R. Sandberg, W. Yang, *et al.*, Atomistic deformation mechanism of silicon under laser-driven shock compression, Nat. Commun. **13**, 5535 (2022).

[95] M. G. Gorman, S. J. Ali, P. M. Celliers, J. L. Peebles, D. J. Erskine, J. M. McNaney, J. H. Eggert, and R. F. Smith, Measurement of shock roughness due to phase plate speckle imprinting relevant for X-ray diffraction experiments on 3rd and 4th generation light sources, J. Appl. Phys. **132**, 175902 (2022).

[96] A. Salamat, R. A. Fischer, R. Briggs, M. I. McMahon, and S. Petitgirard, *In situ* synchrotron x-ray diffraction in the laser-heated diamond anvil cell: Melting phenomena and synthesis of new materials, Coord. Chem. Rev. **277-278**, 15 (2014).

[97] M. G. Gorman, R. Briggs, E. E. McBride, A. Higginbotham, B. Arnold, J. H. Eggert, D. E. Fratanduono, E. Galtier, A. E. Lazicki, H. J. Lee, *et al.*, Direct observation of melting in shock-compressed bismuth with femtosecond X-ray diffraction, Phys. Rev. Lett. **115**, 095701 (2015).

[98] D. Errandonea, High-pressure melting curves of the transition metals Cu, Ni, Pd, and Pt, Phys. Rev. B **87**, 054108 (2013).

[99] S. Singh, R. Briggs, M. G. Gorman, L. X. Benedict, C. J. Wu, S. Hamel, A. L. Coleman, F. Coppari, A. Fernandez-Pañella, C. McGuire, *et al.*, Structural study of hcp and liquid iron under shock compression up to 275 GPa, Phys. Rev. B **108**, 184104 (2023).

[100] S. Singh, M. G. Gorman, P. G. Heighway, J. V. Bernier, D. McGonegle, H. J. Lee, B. Nagler, J. H. Eggert, and R. F. Smith, Unexpected observation of disorder and multiple phase-transition pathways in shock-compressed Zr, Phys. Rev. Lett. **133**, 096101 (2024).

[101] A. Le Bail, H. Duroy, and J. L. Fourquet, *Ab-initio* structure determination of $LiSbWO_6$ by X-ray powder diffraction, Mater. Res. Bull. **23**, 447 (1988).

[102] D. Milathianaki, S. Boutet, G. J. Williams, A. Higginbotham, D. Ratner, A. E. Gleason, M. Messerschmidt, M. M. Seibert, D. C. Swift, P. Hering, *et al.*, Femtosecond visualization of lattice dynamics in shock-compressed matter, Science **342**, 220 (2013).

[103] E. Cid, T. Matsuda, A. Hirose, M. Ohata, T. Terai, T. Kakeshita, Y. Inubushi, T. Sato, K. Miyanishi, M. Yabashi, *et al.*, X-ray free electron laser observation of ultrafast lattice behaviour under femtosecond laser-driven shock compression in iron, Sci. Rep. **13**, 13796 (2023).

[104] A. K. Singh, The lattice strains in a specimen (cubic system) compressed nonhydrostatically in an opposed anvil device, J. Appl. Phys. **73**, 4278 (1993).

[105] A. K. Singh, C. Balasingh, H. K. Mao, R. J. Hemley, and J. Shu, Analysis of lattice strains measured under nonhydrostatic pressure, J. Appl. Phys. **83**, 7567 (1998).

[106] A. K. Singh, C. Balasingh, H.-K. Mao, J. Shut, and R. J. Hemley, Interpretation of the lattice-strains measured under non-hydrostatic pressure, Rev. High Pressure Sci. Technol. **7**, 205 (1998).

[107] H. Wang, D. Wang, L. Hao, J. Li, and H. Y. Geng, High-pressure melting and elastic behavior of vanadium and niobium based on *ab initio* calculations and machine learning molecular dynamics, Phys. Rev. B **112**, 094108 (2025).

[108] J. M. Walsh, M. H. Rice, R. G. McQueen, and F. L. Yarger, Shock-wave compressions of twenty-seven metals. Equations of state of metals, Phys. Rev. **108**, 196 (1957).

[109] R. G. McQueen and S. P. Marsh, Report No. GMX-6-566, Technical Report (Los Alamos Scientific Laboratory, 1964).

[110] L. V. Al'tshuler, A. A. Bakanova, I. P. Dudoladov, E. A. Dynin, R. F. Trunin, and B. S. Chekin, Shock adiabatic curves of metals, J. Appl. Mech. Tech. Phys. **22**, 145 (1981).

[111] R. Smith, J. Eggert, M. Saculla, A. Jankowski, M. Bastea, D. Hicks, and G. Collins, Ultrafast dynamic compression technique to study the kinetics of phase transformations in bismuth, Phys. Rev. Lett. **101**, 065701 (2008).

[112] M. G. Gorman, A. L. Coleman, R. Briggs, R. S. McWilliams, D. McGonegle, C. A. Bolme, A. E. Gleason, E. Galtier, H. J. Lee, E. Granados, *et al.*, Femtosecond diffraction studies of solid and liquid phase changes in shock-compressed bismuth, Sci. Rep. **8**, 16927 (2018).

[113] C. M. Pépin, A. Sollier, A. Marizy, F. Occelli, M. Sander, R. Torchio, and P. Loubeyre, Kinetics and structural changes in dynamically compressed bismuth, Phys. Rev. B **100**, 060101(R) (2019).

[114] T. Epicier and P. Convert, High temperature powder neutron diffraction studies of structural transformations in transition metal hemicarbides M_2C_{1-x}: I. Compounds of the Vth group (V_2C, Nb_2C, Ta_2C), Physica B **156-157**, 41 (1989).

[115] L. Wu, Y. Wang, Z. Yan, J. Zhang, F. Xiao, and B. Liao, The phase stability and mechanical properties of Nb–C system: Using first-principles calculations and nano-indentation, J. Alloys Compd. **561**, 220 (2013).

[116] C. J. Smith, C. R. Weinberger, and G. B. Thompson, Phase stability and microstructural formations in the niobium carbides, J. Eur. Ceram. Soc. **38**, 4850 (2018).

[117] A. B. Belonoshko, T. Lukinov, L. Burakovsky, D. L. Preston, and A. Rosengren, Melting of a polycrystalline material: Melting of real materials, Eur. Phys. J.: Spec. Top. **216**, 199 (2013).

[118] P. F. Weck, J. P. Townsend, K. R. Cochrane, S. D. Crockett, and N. W. Moore, Shock compression of niobium from first-principles, J. Appl. Phys. **125**, 245905 (2019).

[119] J. Byggmästar, K. Nordlund, and F. Djurabekova, Gaussian approximation potentials for body-centered-cubic transition metals, Phys. Rev. Mater. **4**, 093802 (2020).

[120] H. B. Callen, *Thermodynamics and an Introduction to Thermostatistics* (John Wiley & Sons, Hoboken, NJ, 2006).

[121] 10.22003/XFEL.EU-DATA-006659-00.